Observational Requirements for High-Fidelity Reverberation Mapping

Keith Horne,[1,2] Bradley M. Peterson,[3] Stefan J. Collier,[3] and Hagai Netzer [4]

ABSTRACT

We present a series of simulations to demonstrate that high-fidelity velocity-delay maps of the emission-line regions in active galactic nuclei can be obtained from time-resolved spectrophotometric data sets like those that will arise from the proposed *Kronos* satellite. While previous reverberation-mapping experiments have established the size scale R of the broad emission-line regions from the mean time delay $\tau = R/c$ between the line and continuum variations and have provided strong evidence for supermassive black holes, the detailed structure and kinematics of the broad-line region remain ambiguous and poorly constrained. Here we outline the technical improvements that will be required to successfully map broad-line regions by reverberation techniques. For typical AGN continuum light curves, characterized by power-law power spectra $P(f) \propto f^{-\alpha}$ with $\alpha = -1.5 \pm 0.5$, our simulations show that a small UV/optical spectrometer like *Kronos* will clearly distinguish between currently viable alternative kinematic models. From spectra sampled at time intervals Δt and sustained for a total duration $T_{\rm dur}$, we can reconstruct high-fidelity velocity-delay maps with velocity resolution comparable to that of the spectra, and delay resolution $\Delta\tau \approx 2\Delta t$, provided $T_{\rm dur}$ exceeds the broad-line region light crossing time by at least a factor of three. Even very complicated kinematical models, such as a Keplerian flow with superimposed spiral wave pattern, are resolved in maps from our simulated *Kronos* datasets. Reverberation mapping with *Kronos* data is therefore likely deliver the first clear maps of the geometry and kinematics in the broad emission-line regions 1–100 microarcseconds from supermassive black holes.

Subject headings: galaxies: active — galaxies: Seyfert — methods: data analysis — space vehicles: instruments

---

[1]School of Physics and Astronomy, University of St. Andrews, Fife KY16 9SS, Scotland, UK
kdh1@st-and.ac.uk

[2]Department of Astronomy, University of Texas, Austin, TX 78712

[3]Department of Astronomy, The Ohio State University, 140 West 18th Avenue, Columbus, OH 43210
peterson@astronomy.ohio-state.edu,Stefan.Collier@awe.co.uk

[4]School of Physics and Astronomy and The Wise Observatory, Tel Aviv University, Tel Aviv 69978, Israel
netzer@wise.tau.ac.il

1. Introduction

Reverberation mapping (Blandford & McKee 1982; Peterson 1993; Netzer & Peterson 1997) has become part of the standard toolkit for investigation of active galactic nuclei (AGNs). Detailed comparison of broad emission-line flux variations and the continuum variations that drive them can be used to determine the structure and kinematics of the broad-line region (BLR) under a rather simple and straightforward set of assumptions (see Horne 1999 and Peterson 2001 for primers on reverberation mapping). AGN emission lines are observed to respond roughly linearly to continuum variations, each line having a different range of time delays, τ. Since reprocessing times are relatively short, the time delays are dominated by light travel time,

$$\tau = \frac{R}{c}(1 + \cos\theta) \ , \tag{1}$$

where (R,θ,ϕ) are spherical polar coordinates with $\theta = 0$ along our line-of-sight beyond the compact continuum source at $R = 0$. Iso-delay surfaces slice up the geometry of the emission-line region on a set of nested paraboloids. In the simplest linear reprocessing model, the relationship between the continuum light curve, $F_c(t)$, and the emission-line profile variations, $F_\ell(v,t)$, is given by

$$F_\ell(v,t) = \int \Psi_\ell(v,\tau) F_c(t-\tau)\, d\tau \ . \tag{2}$$

The "transfer function," or "velocity-delay map",

$$\Psi_\ell(v,\tau) = \frac{1}{d\tau} \frac{\partial F_\ell(v,t)}{\partial F_c(t-\tau)} \ , \tag{3}$$

is the response at line-of-sight velocity v and time delay τ in the flux of emission line ℓ. The velocity-delay maps of various emission lines code information on the geometry, kinematics, and physical conditions in the BLR (Horne, Korista, & Goad 2003). The immediate goal of reverberation mapping is to recover $\Psi_\ell(v,\tau)$ for each emission line by detailed fitting to variability recorded in high-quality time-resolved spectrophotometric data. The ultimate goal is to unravel the geometry, kinematics, and physical conditions in the BLR.

To date, the great success of reverberation mapping has been determination of the mean broad-line response times for approximately three dozen AGNs, in several cases for multiple lines in a single source (see the compilation of Kaspi et al. 2000). By combining the response times (or "lags") with line widths and assuming that gravity is the dominant force acting on the line-emitting gas, a virial mass for the central black hole can be deduced. Two lines of evidence suggest that these reverberation-based masses are reasonably accurate and actually do measure the black hole mass:

1. For AGNs in which the lags and widths of multiple lines have been measured, there is a clear anticorrelation between Doppler line width Δv and response time τ that is consistent with the virial prediction $\tau \propto \Delta v^{-2}$ since τ measures the light-travel time across the

BLR (Peterson & Wandel 1999, 2000; Onken & Peterson 2002). Lines that arise in higher ionization-level gas (e.g., He II λ1640, N V λ1240) are broader and have shorter response times than lines that arise primarily in lower ionization-level gas (e.g., Hβ, C III] λ1909).

2. Comparison of reverberation-based black-hole masses and host-galaxy bulge velocity dispersons shows a relationship that appears to be the same as the black-hole/bulge velocity-dispersion relationship seen in quiescent galaxies (Ferrarese et al. 2001).

On the other hand, reverberation mapping has not yet achieved the motivating design goal of determining the actual geometry and velocity field of the BLR. This is not surprising since inversion of eq. (2) to solve for the velocity-delay map requires large amounts of high-quality spectra, which are difficult to obtain for AGNs. Published attempts include analyses of NGC 4151 (Ulrich & Horne 1996), NGC 5548 (Wanders et al. 1995; Done & Krolik 1996), and Mrk 110 (Kollatschny 2003), all of which yielded rather ambiguous results. Nevertheless, pursuit of the science goal of determining the BLR structure is important:

1. The origin of the BLR emission remains one of the major mysteries of AGNs. There is no widely accepted paradigm for the nature of the BLR. The BLR clouds may represent the cooler and denser component of a two-phase medium in pressure and virial equilibrium (Krolik, McKee & Tartar 1981). Alternatively, the BLR clouds might be in virial motion, but magnetically confined (Rees 1987). Compelling arguments have been made that the broad emission arises as part of a massive outflow (e.g., Chiang & Murray 1996; Bottorff et al. 1997). Others have suggested that the broad emission arises in the extended atmospheres of stars (e.g., Alexander & Netzer 1997) or at least in part from the surface of the accretion disk itself (e.g., Collin-Souffrin et al. 1988).

2. Knowledge of the BLR structure and kinematics is necessary to understand the potential systematic uncertainties in reverberation-based black-hole masses. This is especially interesting if indeed the outflow models are correct since the virial relationship $\tau \propto \Delta v^{-2}$ is not necessarily expected in simple outflow models. Reverberation-based black-hole masses are now being used to anchor secondary methods of mass determination (e.g., Laor 1998; Wandel, Peterson, & Malkan 1999; Vestergaard 2002; McLure & Jarvis 2002) and it is therefore essential to understand how the measurements are affected by systematics.

Successful reverberation mapping requires a combination of high time resolution, long duration, homogenous high signal-to-noise data, and reasonably high spectral resolution. Precise specification of these quantities depends on physical time scales of the source (e.g., BLR light-crossing time) and the character of the variations, which are neither simple nor regular. This makes experimental design difficult. Nevertheless, the first generation of reverberation experiments have provided a great deal of insight on the continuum and emission-line variability properties of AGNs, making it possible to model their behavior through numerical simulations. Detailed simulations can then be used to determine the observational requirements to map the BLR.

Our main goal in this paper is to describe a program we have undertaken to define the requirements for recovery of high-fidelity velocity-delay maps from data obtained with a small UV/optical spectrophotometer. For the sake of realism, we have used as a model detector system that of a proposed multiwavelength observatory, *Kronos* (Polidan & Peterson 2001; Peterson, Polidan, & Robinson 2003; Peterson, Polidan, & Horne 2004). The wavelength range and resolution and achievable signal-to-noise ratios (S/N) in these simulations are set by the specifications for *Kronos*.

We have carried out two series of simulations, a comparatively simple first series, and a more realistic and complicated second series. The first series of simulations, discussed in §2, addresses the use of velocity-delay maps for a single line, for example the C IV line, to distinguish among several alternative and currently viable models for the geometry and kinematics of the BLR.

The second series, discussed in §3, is intended to be more realistic and challenging. We chose a model with a complicated yet plausible structure, specifically an inclined Keplerian disk with a 2-armed spiral density wave superposed on it. We then used a photoionization equilibrium model appropriate for NGC 5548 (Kaspi & Netzer 1999) to compute the anisotropic emissivity in each line at each point in the disk. In this series of simulations, we considered the response of multiple lines and constructed a model spectrum at each time to determine how blending of closely spaced lines (e.g., Lyα λ1216 and N V λ1240) affect the experimental results.

2. Distinguishing Alternative Geometric and Kinematic Models

2.1. Methodology

Each simulation is based on theoretical velocity-delay maps for one or more emission lines corresponding to a particular model for the BLR, and on fixed observational parameters, e.g., the sampling rate or time resolution Δt, the experiment duration $T_{\rm dur}$, and the S/N per datum. The goal of the simulation is to define the extent to which "observed" velocity-delay maps, reconstructed from the simulated data sets, match the theoretical velocity-delay maps.

Each simulation consists of a number of individual realizations, corresponding to different detailed variations in the driving continuum light curve and different observational errors. For each realization, we (a) generate a model continuum light curve, (b) produce the corresponding model emission-line light curve from the model continuum light curve and the theoretical velocity-delay map, (c) select a simulated data set from pairs of points in the model continuum and emission-line light curves, (d) apply a suitable noise model to the simulated data, and (e) analyze the simulated data set by attempting to recover the velocity-delay map from it. Many such realizations are carried out, and the recovered velocity-delay maps are compared with the original model to assess the fidelity of the process. The individual steps in these simulations are described below.

2.2. Theoretical Velocity-Delay Maps

Theoretical velocity-delay maps were constructed for a variety of models. In the first series of simulations, the velocity-delay maps were selected to be broadly consistent with proposed models for C IV λ1549 in NGC 5548 based on the 1993 intensive monitoring program with *Hubble Space Telescope* (*HST*), the *International Ultraviolet Explorer* (*IUE*), and optical ground-based telescopes (Korista et al. 1995). The specific models we consider are:

A. A spherical distribution of line-emitting clouds in circular Keplerian orbits of random inclination, illuminated by an anisotropic continuum source (Wanders et al. 1995; Goad & Wanders 1996).

B. A flat Keplerian disk of clouds.

C. A hydromagnetically driven wind (Bottorff et al. 1997).

The velocity-delay maps for these models are presented in Fig. 1. A common feature of these models is the broad similarity of their delay maps, i.e., the line response integrated over Doppler velocity

$$\Psi_\ell(\tau) = \int \Psi_\ell(v,\tau)dv, \tag{4}$$

which underscores the importance of making use of both velocity and delay information in determining the BLR structure.

2.3. Model Continuum Variations

The irregular variations of AGN continua can be described in terms of a power-law power-density spectrum

$$P(f) \propto f^{-\alpha}. \tag{5}$$

In our first set of simulations, we generate random light curves with these characteristics by using the method described by White & Peterson (1994) and Peterson et al. (1998). For each realization, a random value of α is selected from a parent distribution with mean value $\mu(\alpha) = 1.5$ and standard deviation $\sigma(\alpha) = 0.5$ (cf. Collier & Peterson 2001 and references therein). Each model light curve is then normalized such that the root-mean-square amplitude of the variations on a one-month time scale is approximately 16%. For the second set of simulations, we used a single light curve generated from a power spectrum with $\alpha = 1$, and normalized to a 30% root-mean-square amplitude on a 200 day timescale. In both cases the resulting model continuum light curves resemble the observed UV continuum variations of well-studied AGNs.

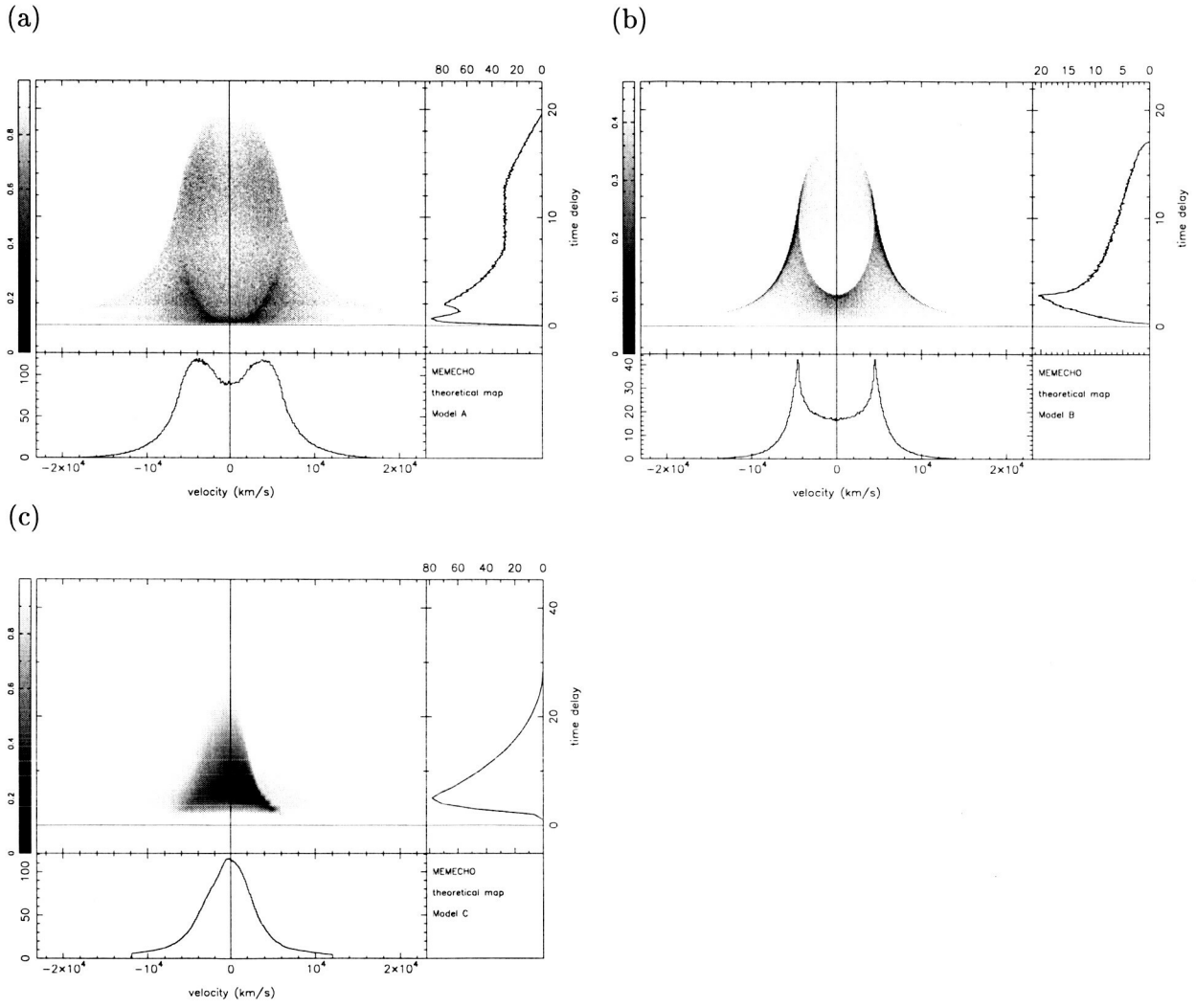

Fig. 1.— Theoretical velocity-delay maps $\Psi_\ell(v,\tau)$ for (a) a spherical distribution of line-emitting clouds in circular Keplerian orbits of random inclination, illuminated by an anisotropic continuum source (Wanders et al. 1995; Goad & Wanders 1996), (b) a flat Keplerian disk of clouds, and (c) a hydromagnetically driven wind (Bottorff et al. 1997). Projections $\Psi_\ell(v)$ and $\Psi_\ell(\tau)$ are shown below and to the right, respectively, of each greyscale $\Psi_\ell(v,\tau)$ map.

2.4. Model Line Response

The line response is computed by convolving the model continuum light curve with the model velocity-delay map, as in eq. (2). This is straightforward provided the delay interval used to sample the velocity-delay map is the same as the time interval Δt of the model light curves. After the convolution, an appropriate number of points at the beginning of the light curve is then removed so that even the first point in the line light curve is fully responding to the continuum variations.

The velocity sampling Δv used for the velocity-delay maps should equal or exceed the spectral resolution of the data. For the first series of simulations, the spectral sampling used was 2 Å (i.e, $\sim 400\,\mathrm{km\,s^{-1}}$ at C IV λ1549). For the second series, we used a spectral sampling roughly matched to the proposed *Kronos* spectrographs, namely 0.7 Å (1 pixel, $135\,\mathrm{km\,s^{-1}}$ at C IV) for the UV lines, and 2.6 Å (1 pixel, 160 $\mathrm{km\,s^{-1}}$ at Hβ). for the optical lines. The resolution actually achieved in the velocity-delay maps cannot exceed Δv and Δt, and is limited by the S/N of the data in comparison with the variations recorded on different timescales in the light curves.

2.5. Sampling the Model Data

For each realization, an artificial data set is created by sampling the model data in such a way as to mimic a real observational program. Our principal goal is to find the combination of time resolution Δt and experiment duration T_{dur} that are required to recover velocity-delay maps at a high level of confidence, so most of the simulations considered various combinations of these two parameters.

In some simulations, we eliminated at random or in groups some fraction of the data points to try to realistically estimate the effect of data losses. We found that for the large data sets that we considered, the results are fairly robust to gaps in the data provided a majority of the data points are retained.

2.6. Simulating Noise

To simulate observational errors, each sampled data point is altered by a random deviate drawn from a Gaussian distribution with a mean of zero and appropriate standard deviation. We assume that the objects to be studied are the relatively bright AGNs that have already been fairly well monitored. For such objects, background noise and readout noise are insignificant and photon shot-noise is the only source of statistical uncertainty. In the case of a small spacecraft-based observatory such as *Kronos*, the limiting photometric accuracy will probably be determined by pointing and guiding errors. We have therefore adopted a very conservative flux minimum uncertainty of 1% for each data point. In the first series of simulations, we assume uncertainties

of $\sim 1\%$ in continuum and $\sim 3\%$ in the emission lines, about the highest precision obtained in previous AGN experiments. In the second series of simulations, the statistical errors are based on the photon-counting statistics for a one-hour exposure with *Kronos*, plus systematic errors (due to spacecraft pointing and jitter) of $\sim 1\%$.

2.7. Velocity-Delay Maps from the Simulated Data

The final step in each simulation is to attempt to recover the velocity-delay map from the simulated data set. This involves solving eq. (2), a classical inversion problem in theoretical physics. In the case of AGN broad-line reverberation, the data are relatively sparse and noisy, and usually irregularly sampled: for this reason, the original Fourier quotient method proposed by Blandford & McKee (1982) has never been applied successfully. These complications motivated development of a number of techniques, superior to Fourier deconvolution, for recovering the observed transfer function $\Psi_\ell(v,\tau)$ from relatively poor quality data. These include the maximum entropy method (MEM) of Horne (1994), the regularized linear inversion (RLI) method of Vio, Horne, & Wamsteker (1994) and Krolik & Done (1995), and the subtractive optimally localized averages (SOLA) method of Pijpers & Wanders (1994).

Our simulations utilize the MEM formalism as implememented in the software package `MEMECHO`, described by Horne (1994). We use `MEMECHO` to fit the data set, defined by the sampled $F_c(t)$ and $F_\ell(v,t)$, with a linearized echo-mapping model

$$F_\ell(v,t) = \bar{F}_\ell(v) + \int_0^\infty \Psi_\ell(v,\tau)\,[F_c(t-\tau) - \bar{F}_c]\,d\tau\ . \tag{6}$$

This differs from the linear model of eq. (2) by the inclusion of "background" fluxes $\bar{F}_c$ for the continuum, and $\bar{F}_\ell(v)$ for the line profile. These backgrounds account for approximately time-independent contaminating fluxes, including the host-galaxy starlight contribution to the continuum and narrow emission-line flux in the core of the emission line profile. We set the backgrounds to the mean line and continuum levels in the data. The velocity-delay map $\Psi_\ell(v,\tau)$ in the above model then represents the marginal responsivity (i.e., relative to the background levels) to changes in the continuum. The linearized echo-mapping model is thus insensitive to mild non-linear line responsivities and affords an improvement over the simpler linear model of eq. (2). The MEM fit proceeds iteratively, by varying model $F_c(t)$, $\Psi_\ell(v,\tau)$, and $\bar{F}_\ell(v)$ to fit simultaneously the observed $F_c(t)$ and $F_\ell(v,t)$. The "smoothest positive maps", i.e., the maps which maximize the entropy, for which $\chi^2/N \approx 1 \pm \sqrt{2/N}$, with N the number of line and continuum measurements, defines a satisfactory fit to the data. The "observed" velocity-delay map $\Psi_\ell(v,\tau)$ that is recovered from the simulated data is then compared with the original model velocity-delay map.

2.8. Discussion of Results

Our first series of simulations has been described in some detail in a conference proceedings (Collier, Peterson, & Horne 2001), so here we report on some highlights that illustrate our general conclusions.

Our first general finding supports the "rule of thumb" (e.g., Press 1978) that the time series should be at least three times longer than the maximum time scale to be probed. The BLR models used here have an outer radius $R_{\rm out} \approx 10$ light days (varying slightly for the particular models) so the longest timescale for response is $2R_{\rm out}/c \approx 20$ days. The velocity-delay maps recovered from the simulated data became recognizable and distinguishable from one another only with $\gtrsim 60$ days of data, regardless of how fine a sampling grid is used.

In Fig. 2, we show the "observed" velocity-delay maps recovered from a simulation with duration $T_{\rm dur} = 60$ days and time resolution $\Delta t = 0.1$ day (i.e., at total of ~ 600 observations). In comparison with the corresponding theoretical maps in Fig. 1, these "observed" maps are clearly somewhat blurred in both the delay and velocity dimensions. The finite resolution of the reconstructed maps is a limiting factor in their ability to distinguish among alternative geometric and kinematic models of the BLR. High resolution maps require good sampling in time and velocity, and a sufficient signal-to-noise in the observations to detect the possibly quite small brightness changes that provide the information that defines the maps. Comparison of Figs.1 and 2 indicates that the resolution achieved in Fig. 2 is about 1 day in τ and a few hundred km s^{-1} in v. We consider this to be adequate to distinguish among the three models shown.

For somewhat coarser time resolution, longer durations are required to achieve comparable fidelity, though fewer data points suffice: for results similar in quality to those shown in Fig. 2, $\Delta t = 0.5$ day requires $T_{\rm dur} \approx 80$ days (~ 400 observations) and $\Delta t = 1$ day requires $T_{\rm dur} \approx 100$ days (~ 100 observations). However, further increases in Δt resulted in unacceptable loss of delay resolution in the velocity-delay map; in these simulations the shortest time scales of interest were of order 2 days, so the resolution of the monitoring experiment must be finer than this.

At first glance, it appears that these requirements have been *nearly* met in previous reverberation-mapping programs, most notably the 1996 *IUE* campaign on NGC 7469 (Wanders et al. 1997), which arguably represents the current state of the art. We test the verisimilitude of our simulations by reproducing the characteristics of this previous observing campaign.

We therefore carried out the same simulation process, with minor changes made to mimic the characteristics of the *IUE* data. Specifically, we adopted the following parameters: (a) $T_{\rm dur} = 49$ days, (b) $\Delta t = 0.2$ days, (c) continuum and emission-line flux uncertainties of 3% and 7%, respectively, (d) spectral resolution ~ 8 Å, and (e) continuum variations normalized to an amplitude of 12% on timescales of 10 days. We show the results of these simulations for two of our model velocity-delay maps in Fig. 3, which should be compared with the corresponding models in Fig. 1. The delay resolution of these maps is now ~ 5 days, owing mainly to the lower S/N

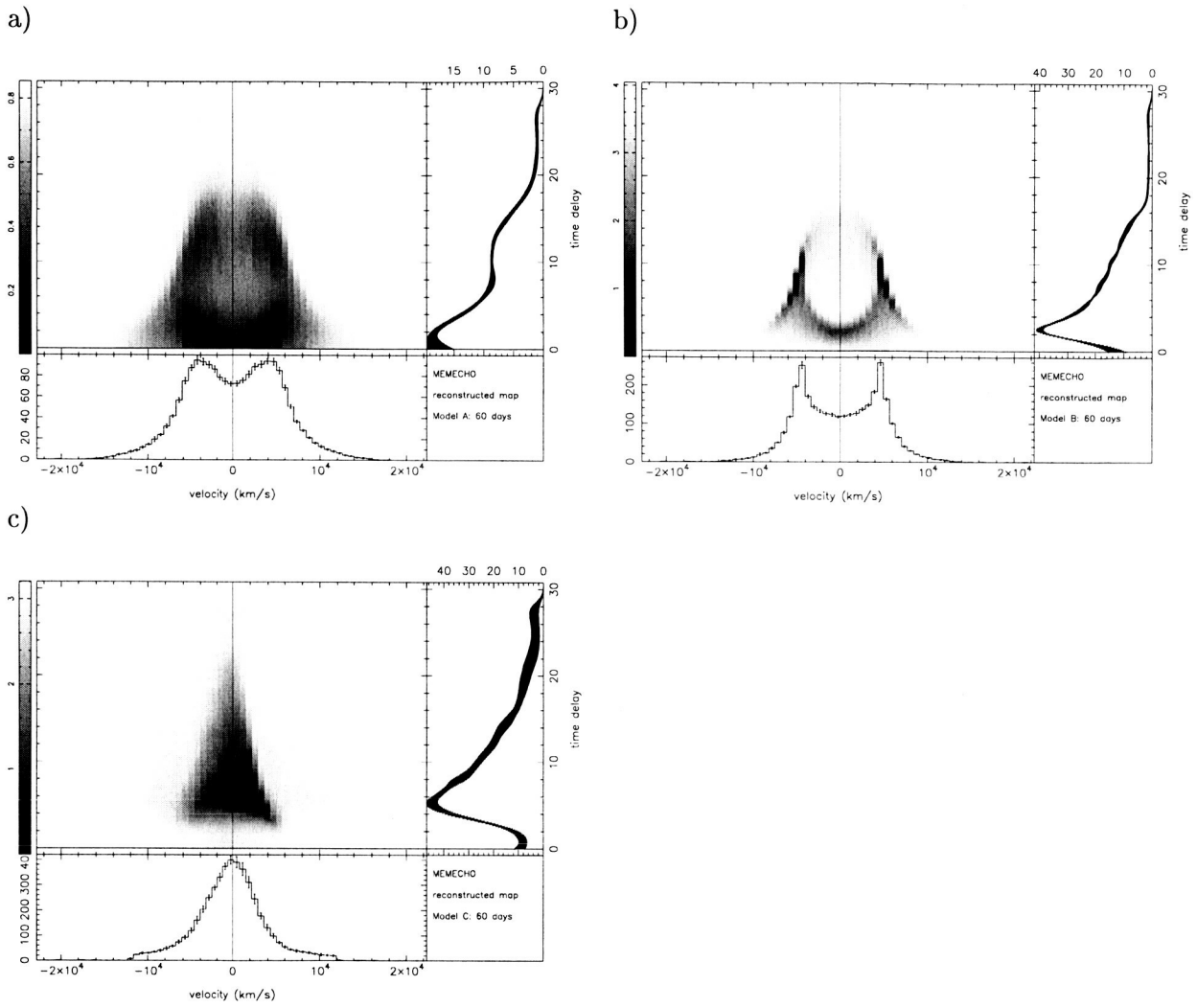

Fig. 2.— Observed velocity-delay maps $\Psi_\ell(v,\tau)$ recovered from a simulation with duration $T_{\rm dur} = 60\,{\rm days}$ and time resolution $\Delta t = 0.1\,{\rm day}$ (i.e., at total of ~ 600 observations). As in Fig. 1, the three cases shown are for (a) a spherical distribution of line-emitting clouds in circular Keplerian orbits of random inclination, illuminated by an anisotropic continuum source (Wanders et al. 1995; Goad & Wanders 1996), (b) a flat Keplerian disk of clouds, and c) a hydromagnetically driven wind (Bottorff et al. 1997). Projections $\Psi_\ell(v)$ and $\Psi_\ell(\tau)$, with Monte Carlo error bars, are shown below and to the right, respectively, of each greyscale $\Psi_\ell(v,\tau)$ map.

compared with the maps in Fig. 2. The quality of the velocity-delay maps that we obtain in these simulations is similar to the quality of the velocity-delay maps recovered from the real data. It is clear that the recovered velocity-delay maps based on simulations using *IUE*-like parameters do not have sufficient S/N and/or duration to distinguish between these two competing BLR models.

3. Simulations of a Photoionized Disk with Spiral Arms

The second series of simulations is intended to be more challenging: the simulated data are more realistic and the BLR structure is chosen to be rather complicated. The precise nature of the BLR structure is less important than the fact that it is complex: the desired demonstration is that a complex system can be successfully mapped.

3.1. Spiral Disk Kinematics

In these simulations, the BLR model we adopted is a population of 10^5 discrete gas clouds on elliptical Keplerian orbits around a black hole of mass $3 \times 10^7\ M_\odot$. The orbital semi-major axes a are populated with gas clouds uniformly distributed in $\log a$ from $a_{\rm in} = 3$ to $a_{\rm out} = 50$ light days. The orbits all lie in a plane inclined at $i = 45^\circ$ to the line of sight.

To generate a spiral wave pattern on the Keplerian disk, we make the orbits elliptical, in this case eccentricity $e = 0.3$, and we "twist" the orbits by advancing the azimuth θ of the major axis with $\log a$:

$$\theta_0(a) = \theta_{\rm in} + \ln\left(\frac{a_{\rm in} - a}{\Delta a}\right) . \tag{7}$$

The orbiting gas clouds spend most of their time near the apbothron, at $(R, \theta) = (a/(1-e), \theta_0(a))$. The twisting set of elliptical orbits thus generates a trailing spiral wave pattern, with the surface density of clouds on the face of the disk enhanced near

$$R(\theta) = \frac{a_{\rm in} - \Delta a\ \exp\{\theta - \theta_{\rm in}\}}{1 - e} . \tag{8}$$

To produce two such spiral arms, we simply rotate the orientation of the orbit of each cloud by 180° with 50% probability.

3.2. Physical Conditions in the Model BLR

Physical conditions in the clouds vary with their radial distance R from the nucleus. We adopt a power-law model similar to that which Kaspi & Netzer (1999) employed in their attempt to fit the observed behavior of NGC 5548 during the 1989 monitoring campaign by the International

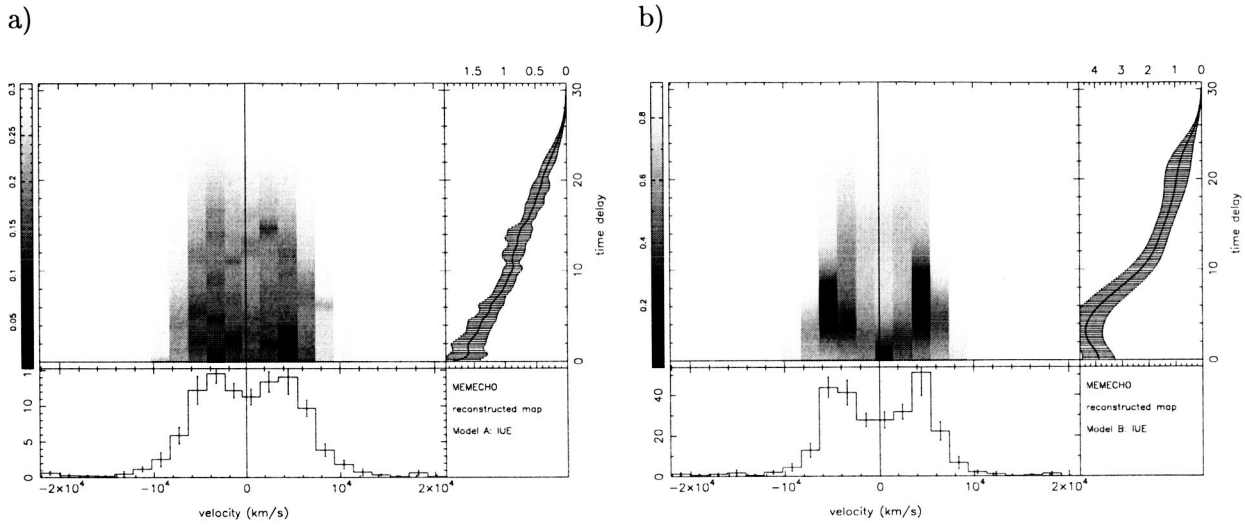

Fig. 3.— Observed velocity-delay maps $\Psi_\ell(v,\tau)$ recovered from simulated data with characteristics similar to continuous *IUE* monitoring, specifically, $T_{\rm dur} = 49$ days, $\Delta t = 0.2$ days, continuum and emission-line flux uncertainties of 3% and 7%, respectively, spectral resolution ~ 8 Å, and continuum variations normalized to an amplitude of 12% on timescales of 10 days. The two cases shown, as in Fig. 1, are (a) a spherical distribution of line-emitting clouds in circular Keplerian orbits of random inclination, illuminated by an anisotropic continuum source (Wanders et al. 1995; Goad & Wanders 1996), and (b) a flat Keplerian disk of clouds. Projections $\Psi_\ell(v)$ and $\Psi_\ell(\tau)$, with Monte Carlo error bars, are shown below and to the right, respectively, of each greyscale $\Psi_\ell(v,\tau)$ map.

AGN Watch (Clavel et al. 1991; Peterson et al. 1991). The gas density is uniform inside a given cloud, and differs from cloud to cloud, decreasing outward as

$$n = n_1 \left(\frac{R}{R_1}\right)^{-s} , \tag{9}$$

where we adopt $s = 1$ for the density exponent and $n_1 = 10^{11.4}\,\mathrm{cm}^{-3}$ for the density at the fiducial radius $R_1 = 10^{15.4}\,\mathrm{cm} = 1$ light day. Note that R varies from $a/(1+e)$ to $a/(1-e)$, and the density of a given cloud varies accordingly, as the cloud traverses its elliptical orbit. The column density is similarly given by

$$N = N_1 \left(\frac{R}{R_1}\right)^{-2s/3} , \tag{10}$$

with $N_1 = 10^{24}\,\mathrm{cm}^{-2}$, and the corresponding ionization parameter is

$$U \equiv \frac{Q}{4\pi c R^2 n} = U_1 \left(\frac{R}{R_1}\right)^{s-2} , \tag{11}$$

where $U_1 \approx 10^{0.2}$ for the adopted mean ionizing photon rate, $\bar{Q} = 10^{54}$ photons s^{-1}. For $3 < R/R_1 < 50$, we have $10.92 \geq \log n \geq 9.40$, $23.68 \geq \log N \geq 22.67$, and $-0.28 \geq \log U \geq -1.80$. This model roughly reproduces the emission line ratios observed in NGC 5548.

Individual clouds have a projected area $A \propto (N/n)^2 \propto R^{2s/3}$, and therefore cover a solid angle $\Omega = A/R^2 \propto R^{\frac{2s}{3}-2} \propto R^{-4/3}$ as viewed from the nucleus. We normalize the cloud population by summing over all clouds to obtain a total solid angle $\sum_i \Omega_i = 4\pi f$, and set the total covering fraction to $f = 0.3$. This simply scales the model line fluxes to roughly reproduce those observed in NGC 5548 (Kaspi & Netzer 1999).

Our assumed thin disk geometry is probably inconsistent with so large a covering fraction as $f = 0.3$, unless anisotropic emission or scattering of the ionizing radiation increases its probability of crossing the disk plane. Obscuration of one cloud by another is also ignored. We largely overlook these issues here, because our main purpose is not to produce the most realistic BLR model, but rather to check the ability of *Kronos* to recover rich structure in the velocity-delay map of a complicated BLR.

3.3. Reprocessing by the Photoionized Gas Clouds

We employ the photoionization model `ION` (Kaspi & Netzer 1999 and references therein) to compute inward and outward emission-line fluxes, $F_\ell^-(n, N, U)$ and $F_\ell^+(n, N, U)$, as functions of density n, column density N, and ionization parameter U. For intermediate viewing angles we interpolate linearly in $\cos\theta$:

$$F_\ell(\theta) = \left(\frac{F_\ell^+ + F_\ell^-}{2}\right) + \left(\frac{F_\ell^+ - F_\ell^-}{2}\right)\cos\theta . \tag{12}$$

To save computer time, we pre-compute the inward and outward fluxes for each line on a 3-dimensional grid spanning $7.5 \leq \log n \leq 13$, $19 \leq \log N \leq 23.4$, and $-3.5 \leq \log U \leq 0.25$, at intervals $\Delta \log n = 0.5$, $\Delta \log N = 0.4$, and $\Delta \log U = 0.25$, respectively. We interpolate in this grid to compute line fluxes contributed by each cloud at each location in its orbit in each of five key emission lines, Lyα, N V λ1240, C IV λ1549, He II λ1640, and Hβ.

3.4. Theroetical Velocity-Delay Maps

Figure 4 shows a color representation of the spiral disk BLR model projected on the sky, and the corresponding velocity-delay map. To generate these color representations we superimpose the responses of three different emission lines, Lyα, C IV, and He II, in red, blue, and green, respectively. The two spiral arms clearly visible on the sky view are easily traced on the velocity-delay map. The vivid colors apparent in both the sky view and the velocity-delay map arise because each line probes a different range of physical conditions and ionization level. The He II zone, for example, is more tightly confined to the vicinity of the nucleus. The front-to-back asymmetry reflects different anisotropies in the emission of different lines; the Lyα emission, in particular, is stronger on the far side of the nucleus.

3.5. Ionizing and Continuum Light Curves

Variations in the ionizing radiation are generated by using a random walk in time, which has a power spectrum $P(f) \propto f^{-1}$. We first standardize the random walk by subtracting its mean and dividing by its standard deviation, evaluated at the times of observations, to obtain a function $\eta(t)$ with mean 0 and standard deviation 1. We can then scale $\eta(t)$ to match the desired mean $\bar{Q}$ and amplitude ΔQ of the variable ionizing radiation. To ensure that $Q(t)$ can never become negative, we take

$$Q(t) = \bar{Q}\ \exp\{\Delta Q\ \eta(t)/\bar{Q}\} \approx \bar{Q} + \Delta Q\ \eta(t)\ . \tag{13}$$

For these simulations we take $\bar{Q} = 10^{54}$ photons s^{-1} for the mean ionizing photon rate, and $\Delta Q = 0.3\bar{Q}$ for the root-mean-square amplitude of the variations in ionizing flux over the 200-day period.

We assume that the UV and optical continuum variations $F_c(\lambda, t)$ are proportional to the ionizing photon variations $Q(t)$,

$$F_c(\lambda, t) = \bar{F}_c(\lambda)\ \exp\{\Delta F_c(\lambda)\ \eta(t)/\bar{F}_c(\lambda)\} \approx \bar{F}_c(\lambda) + \Delta F_c(\lambda)\ \eta(t)\ . \tag{14}$$

Here $\bar{F}_c(\lambda)$ and $\Delta F_c(\lambda)$ are the mean and root-mean-square continuum spectra, for which we adopt power-law forms matched to the observed mean and root-mean-square flux variations in the continuum of NGC 5548 at 135 nm and 510 nm. Note that the UV and optical continua may arise in part from reprocessing of harder photons, and hence may exhibit a wavelength-dependent range

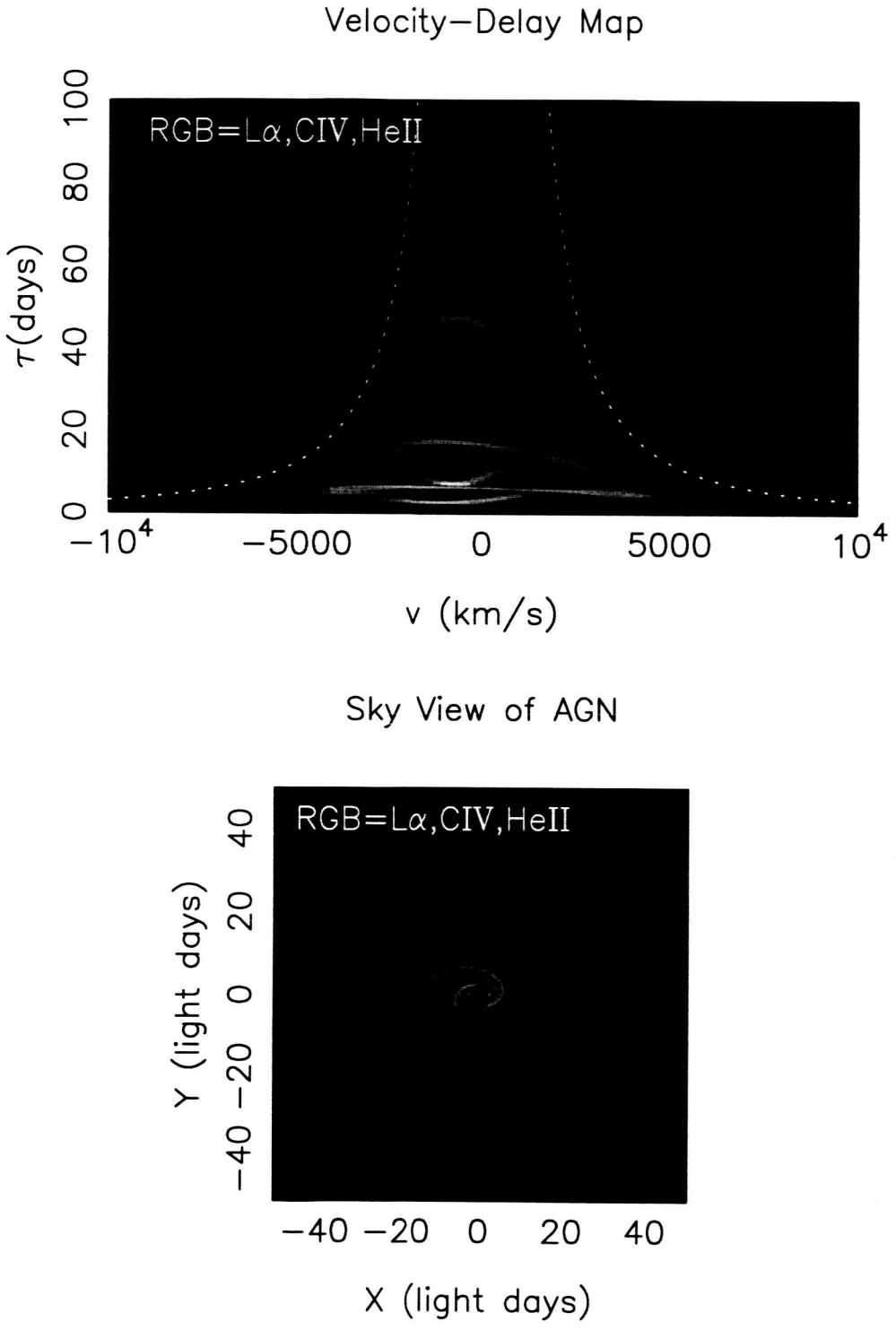

Fig. 4.— Velocity-delay map and corresponding sky view for a Keplerian accretion disk with two spiral arms. Red, green, and blue correspond to the Lyα, C IV, and He II emission lines, respectively.

of time delays. For the present simulations we neglect this possibility, since the continuum time delays are much smaller than those in the emission lines.

3.6. Synthetic *Kronos* Spectra

In addition to using the photoionization model to account for the non-linear and anisotropic responses of each cloud to the ionizing radiation, Doppler shifts and time delays are taken into account when adding to the spectrum at each time the line emission contributions from each gas cloud:

$$F_\ell(v,t) = \sum_i \frac{A_i F_\ell\left(\theta_i, n_i, N_i, U_i(t)\right)}{D_L^2(z)} \frac{\exp\left\{-\frac{1}{2}\left(\frac{v-v_i}{\Delta v_i}\right)^2\right\}}{\sqrt{2\pi}\Delta v_i} \ , \tag{15}$$

where z is the redshift, and $D_L(z)$ the luminosity distance. At time t, cloud i, with density n_i, column density N_i and area A_i, is located at R_i, θ_i, and has an ionization parameter $U_i(t) = Q(t-\tau_i)/4\pi c R_i^2 n_i$, where the light travel time delay is $\tau_i = (R_i/c)(1+\cos\theta_i)$. In addition to the orbital Doppler shift, v_i, each cloud is given a velocity dispersion $\Delta v_i = 0.1$ times the local Keplerian orbital velocity.

Synthetic spectra are generated using the design spectral range, resolution, and wavelength-dependence sensitivity of the *Kronos* spectrometers (Polidan & Peterson 2001). Specifically, we assume UV and NUV/Opt spectrographs covering 100–175 nm with 1100 pixels and 270–540 nm with 2000 pixels, respectively. The noise model adopted in the simulations is based on photon-counting statistics, assuming an exposure time of 3600 s, systematic errors of 1%, and wavelength-dependent effective area $A_{\rm eff}(\lambda)$ interpolated in wavelength from the values given in Table 1.

The quality of AGN spectra that will be obtained by *Kronos* in a 1-hour exposure on

Table 1. *Kronos* Spectrographs

λ (nm)	$A_{\rm eff}$ (cm^2)	Δv (km s^{-1}pix^{-1})	λ (nm)	$A_{\rm eff}$ (cm^2)	Δv (km s^{-1}pix^{-1})
100	232	225	270	584	150
112	299	200	300	623	135
125	259	180	350	600	116
150	154	150	400	675	101
160	112	140	450	668	90
175	72	129	500	567	81
			540	510	75

NGC 5548 is indicated in Fig. 5. Here the top spectrum is our synthetic spectrum for a single 1-hour integration obtained near peak brightness. Below this (with much less noise) are the mean and root-mean-square of 1001 such synthetic spectra, from a simulation with $\Delta t = 0.2$ day and $T_{\rm dur} = 200$ days.

3.7. Recovery of Delay Maps

To extract continuum and emission-line light curves from the synthetic spectra, we employ the same code that we use to measure real spectra. A power-law continuum is fitted to each synthetic spectrum, and light curves for the continuum and continuum-subtracted line fluxes are measured from the spectra. `MEMECHO` is then used to fit the measured UV continuum light curve and the continuum-subtracted light curves of each emission line. As shown in Fig. 6, this fit reproduces the observed continuum variations and the variously time-delayed line flux variations, recovering a delay map $\Psi_\ell(\tau)$ for each line.

3.8. Recovery of Velocity-Delay Maps

Finally, the continuum-subtracted line variations are measured for typically 100 bins across the velocity profile of each emission line. A `MEMECHO` fit then recovers a velocity-delay map $\Psi_\ell(v,\tau)$ for each line. The results are shown in Fig. 7. The spiral patterns are clearly visible in both the sky views and the theoretical velocity-delay maps. The reconstructed maps are again blurred in τ and v, due to the finite resolution of the mapping procedure, but the spirals are clearly recovered for the strong Lyα, C IV, and Hβ lines, and incipient structure is apparent even in the weaker, rapidly responding He II line.

As with the first set of simulations, we find that when we increase Δt, we must compensate by increasing $T_{\rm dur}$ to recover velocity-delay maps of comparable fidelity. This enables mapping over time delays longer than $\sim 2\Delta t$ with a smaller total number of spectra. However, the structure lost on short time scales leads to highly indeterminate results for rapidly responding lines like He II. Furthermore, there are few AGNs that can be observed continuously for periods longer than ~ 200 days with an Earth-orbiting observatory without the target getting too close to the Sun for observation.

4. Discussion

The major result of this investigation is a clear demonstration that with technically realizable observational programs reverberation mapping can successfully recover even complex emission-line velocity-delay maps.

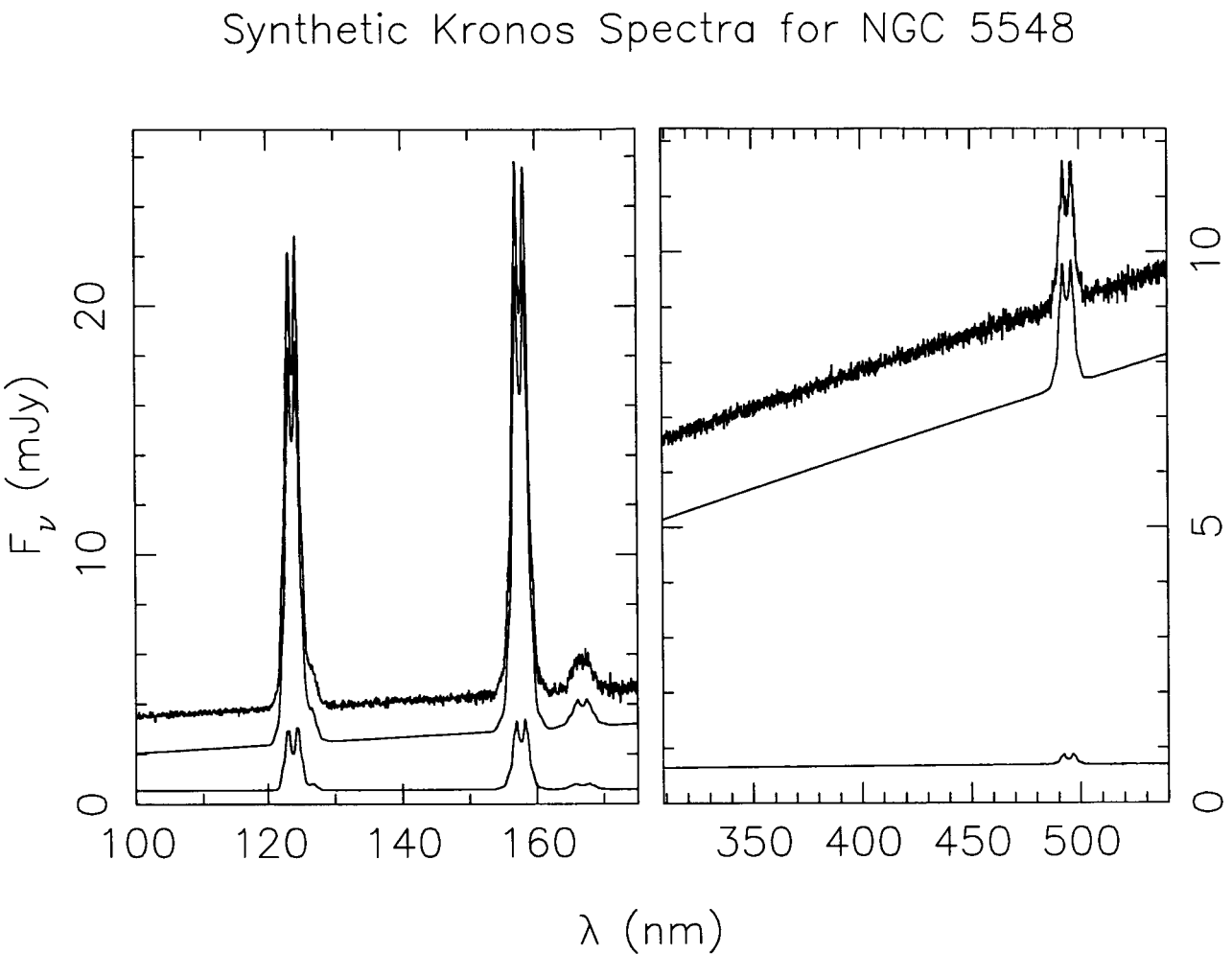

Fig. 5.— Synthetic *Kronos* spectra for NGC 5548. Top spectrum is a single 1-hour integration near peak brightness, below which are the mean and root-mean-square of 1001 such spectra, representing 1-hour integrations every 0.2 days for 200 days. This simulation of reverberation in the environment of a $10^7 M_\odot$ black hole includes a Keplerian disk with spiral density waves, continuum variations, and responses in five key emission lines, Lyα, N V λ1240, C IV λ1549, He II λ1640, and Hβ.

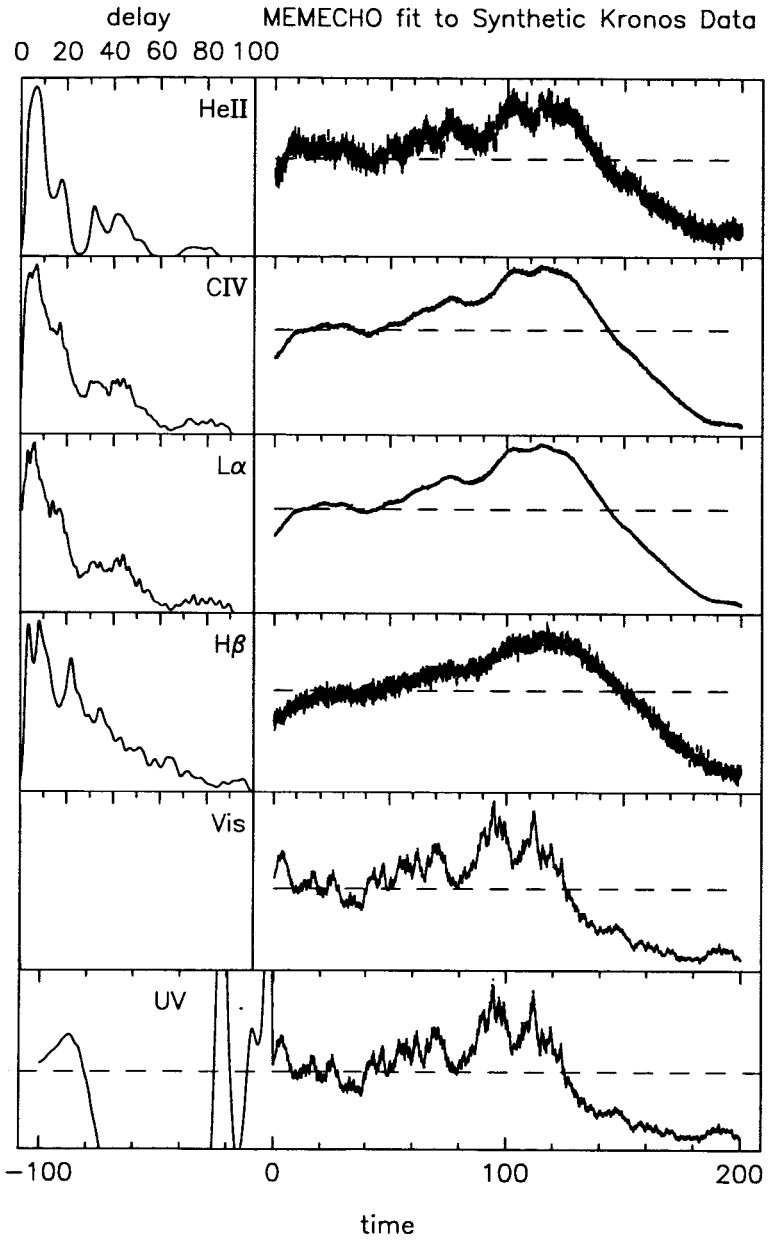

Fig. 6.— Continuum and velocity-integrated emission line fluxes measured from simulated *Kronos* spectra, representing 1-hour integrations every 0.2 days for 200 days. The driving continuum light curve $F_c(t)$ is in the bottom panel, the responding line light curves $F_\ell(t)$ above, and the recovered delay maps $\Psi_\ell(\tau)$ are shown in the left-hand column.

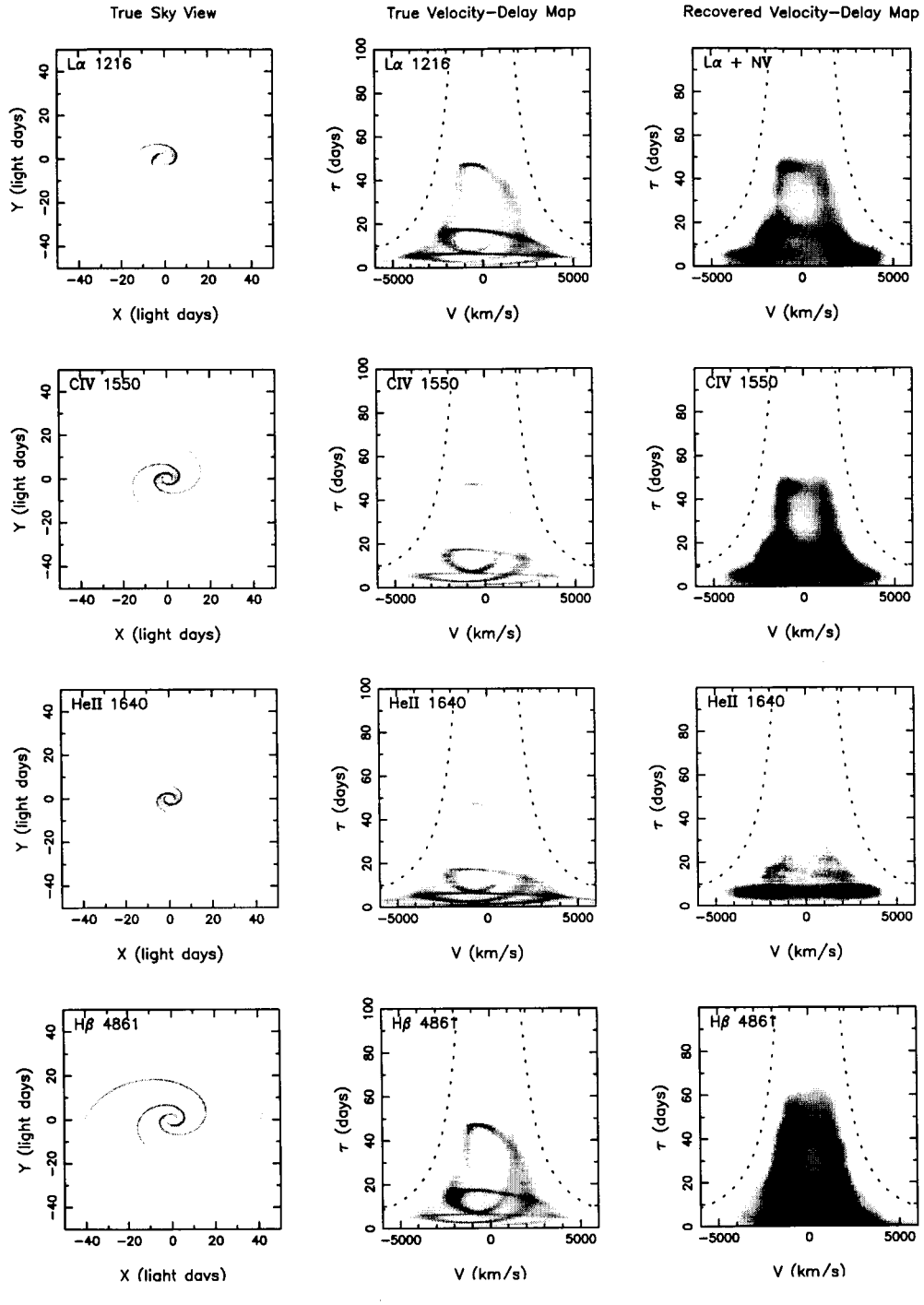

Fig. 7.— Recovery of velocity-delay maps from simulated *Kronos* data sets. The left column shows "sky views" of the adopted BLR model, in this case a Keplerian accretion disk with two spiral arms, in the light of four different emission lines. The middle column shows the corresponding theoretical velocity-delay maps, in which the spiral arms are also clearly visible. The right column gives the "observed" velocity-delay maps recovered from simulated *Kronos* data representing 1-hour exposures every 0.2 days for 200 days.

Previous reverberation mapping programs have had comparatively modest goals: generally, the intent has been to measure the mean response time for various emission lines. From these programs, we have learned enough about AGN continuum and emission-line variability characteristics to carry out realistic simulations, such as those described here, that will define future programs with more ambitious goals. These simulations show clearly that even the most ambitious previous programs could not be expected to yield the results we now seek, i.e., a complete velocity-delay map that can be used to identify the detailed structure and kinematics of the BLR.

We also conclude from these simulations that while high-fidelity reverberation mapping of even a single line will be a tremendous step forward, this will not yield the complete structure of the BLR. This is clearly illustrated in Fig. 4, where the vivid colors arise because different emission lines probe different ranges of physical conditions and ionization level. To acquire a complete picture of the BLR, a variety of lines spanning a broad range of ionization level (and hence mean response time) need to be mapped. Moreover, it is distinctly possible that the high-ionization and low-ionization lines arise primarily in physically distinct regions with different geometries and kinematics (e.g., Collin-Souffrin et al. 1988); if this is true, the need for reverberation mapping of multiple emission lines is self-evident.

Once we have acquired the data to make high-fidelity velocity-delay maps for different emission lines, how can we produce a map of the BLR? Perhaps the simplest approach is though inspired modeling: practitioners recognizing the structure in the velocity-delay maps can devise appropriate models with adjustable parameters to obtain the best fit of a model to the data. A more ambitious program aims to reconstruct a complete phase-space map from the velocity-delay maps of different lines, or even directly from the data. This may be problematic, however, because the "observable" velocity-delay map is a two-dimensional projection of the six-dimensional phase space, so there are degeneracies. These can be partially resolved by combining results from multiple lines with photoionization equilibrium models, and some success has already been achieved with simple geometries (Horne 2001; Horne, Korista, & Goad 2002). Such methods will succeed best if the BLR structure has some degree of simplifying symmetry, as we expect from most current models. But even if the BLR is completely chaotic with no symmetries, this could be concluded from good reverberation data, and would provide us with an important answer about the inner structure of AGNs.

We are grateful to NASA for support of this work through LTSA Grant NAG5–8397 to The Ohio State University. KH was supported by a PPARC Senior Fellowship, and by a Beatrice Tinsley Visiting Professorship at the University of Texas at Austin. We thank Mark Bottorff for supplying the model transfer function shown in Fig. 1c. We thank F.P. Pijpers and K.T. Korista for helpful comments on the manuscript.

REFERENCES

Alexander, T., & Netzer, H. 1997, MNRAS, 284, 967

Blandford, R., & McKee, C.F. 1982, ApJ, 255, 419

Bottorff, M., Korista, K.T., Shlosman, I., & Blandford, R.D. 1997, ApJ, 479, 200

Chiang, J., & Murray, N. 1996, ApJ, 466, 704

Clavel, J., et al. 1991, ApJ, 366, 64

Collier, S., & Peterson, B.M. 2001, ApJ, 555, 775

Collier, S., Peterson, B.M., & Horne, K. 2001, in Probing the Physics of Active Galactic Nuclei by Multiwavelength Monitoring, ed. B.M. Peterson, R.S. Polidan, & R.W. Pogge, (San Francisco: Astronomical Society of the Pacific), p. 457

Collin-Souffrin, S., Dyson, J.E., McDowell, J.C., Perry, J.J. 1988, MNRAS, 232, 539

Done, C., & Krolik, J.H. 1996, ApJ, 463, 144

Ferrarese, L., Pogge, R.W., Peterson, B.M., Merritt, D., Wandel, A., & Joseph, C.L. 2001, ApJ, 555, L79.

Goad, M., & Wanders, I. 1996, ApJ, 469, 113

Horne, K. 1994, in Reverberation Mapping of the Broad-Line Region in Active Galactic Nuclei, ed. P.M. Gondhalekar, K. Horne, & B.M. Peterson, (San Francisco: Astronomical Society of the Pacific), p. 23

Horne, K. 1999, in Quasars and Cosmology, ed. G. Ferland & J. Baldwin, (San Francisco: Astronomical Society of the Pacific), p. 189

Horne, K. 2001, in Probing the Physics of Active Galactic Nuclei by Multiwavelength Monitoring, ed. B.M. Peterson, R.S. Polidan, & R.W. Pogge, (San Francisco: Astronomical Society of the Pacific), p. 387

Horne, K., Korista, K.T., & Goad, M.R. 2003, MNRAS, 339, 367

Kaspi, S., & Netzer, H. 1999, ApJ, 524, 71

Kaspi, S., Smith, P.S., Netzer, H., Maoz, D., Jannuzi, B.T., & Giveon, U. 2000, ApJ, 533, 631

Kollatschny, W. 2003, A&A, 407, 461

Korista, K.T., et al. 1995, ApJS, 97, 285

Krolik, J.H., & Done, C. 1995, ApJ, 440, 166

Krolik, J.H., McKee, C.F., Tarter, C.B. 1981, ApJ, 249, 422

Laor, A. 1998, ApJ, 505, L83

McLure, R.J., & Jarvis, M.J. 2002, MNRAS, 337, 109

Netzer, H., & Peterson, B.M. 1997, in Astronomical Time Series, ed. D. Maoz, A. Sternberg, & E.M. Leibowitz, (Dordrecht: Kluwer), p. 85

Onken, C.A., & Peterson, B.M. 2002, ApJ, 572, 746

Peterson, B.M. 1993, PASP, 105, 247

Peterson, B.M. 2001, in Advanced Lectures on the Starburst–AGN Connection, ed. I. Aretxaga, D. Kunth, & R. Mújica, (Singapore: World Scientific), p. 3

Peterson, B.M., Polidan, R.S., & Robinson, E.L. 2003, in Future EUV/UV and Visible Space Astrophysics Missions and Instrumentation, ed. J.C. Blades & O.H.W. Sigmund, Proceedings of the SPIE, Vol. 4854, p. 311

Peterson, B.M., Polidan, R.S., & Horne, K. 2004, Astron. Nachr. 325, in press

Peterson, B.M., & Wandel, A. 1999, ApJ, 521, L95

Peterson, B.M., & Wandel, A. 2000, ApJ, 540, L13

Peterson, B.M., et al. 1991, ApJ, 368, 119

Peterson, B.M., Wanders, I., Horne, K., Collier, S., Alexander, T., Kaspi, S., & Maoz, D. 1998, PASP, 110, 660

Pijpers, F.P., & Wanders, I. 1994, MNRAS, 271, 183

Polidan, R.S., & Peterson, B.M. 2001, in Probing the Physics of Active Galactic Nuclei by Multiwavelength Monitoring, ed. B.M. Peterson, R.S. Polidan, & R.W. Pogge, (San Francisco: Astronomical Society of the Pacific), p. 479

Press, W. 1978, Comments on Ap., 7, 103

Rees, M.J. 1987, MNRAS, 228, 47P

Ulrich, M.-H., & Horne, K. 1996, MNRAS, 283, 748

Vestergaard, M. 2002, ApJ, 571, 733

Vio, R., Horne, K., & Wamsteker, W. 1994, PASP, 106, 1091

Wandel, A., Peterson, B.M., & Malkan, M.A. 1999, ApJ, 526, 579

Wanders, I., Goad, M.R., Korista, K.T., Peterson, B.M., Horne, K., Ferland, G.J., Koratkar, A.P., Pogge, R.W., & Shields, J.C. 1995, ApJ, 453, L87

Wanders, I., et al. 1997, ApJS, 113, 69

White, R.J., & Peterson, B.M. 1994, PASP, 106, 879

This preprint was prepared with the AAS LaTeX macros v4.0.